Carbon 196 (2022) 466–473

Contents lists available at ScienceDirect

Carbon

journal homepage: www.elsevier.com/locate/carbon

Monoatomic tantalum induces ordinary-pressure phase transition from graphite to n-type diamond

Chengke Chen [1], Dong Fan [1], Hui Xu, Meiyan Jiang, Xiao Li, Shaohua Lu, Changcheng Ke, Xiaojun Hu [*]

College of Materials Science and Engineering, Zhejiang University of Technology, Hangzhou, 310014, PR China

ARTICLE INFO

Keywords:
Diamond
Graphite
Phase transition
Monoatomic tantalum
n-type conductivity

ABSTRACT

It is a key challenge to synthesize large-area n-type diamond, which significantly obstacles its application in electronic devices. Here we find that monoatomic tantalum (Ta) lets graphite transform to diamond under normal pressure, subverting the common sense that this transition needs high temperature and high pressure, opening an era for preparing large-area diamond based on large-sized graphite. This phase transition removes non-diamond component in grain boundaries forming closely-packed nanocrystalline diamond films and terminates the grains by Ta, producing high mobility n-type conductivity. First principle calculations reveal that Ta supplies electrons to the adjacent graphene layer, transforming sp^2 electronic configuration to sp^3 state with energy barrier of −5.38 eV/unit cell. Ta terminated diatomic layer diamond forms a shallow donor energy level of ~0.4 eV. This supplies important significance in the fabrication of diamond-based electronic devices and gives a way for the sp^2/sp^3 hybridized matter to realize the phase transition under ordinary pressure.

1. Introduction

Diamond was regarded as a technologically attractive material for a variety of electronic applications due to its unique properties such as wide band gap, high carrier mobility and high thermal conductivity [1–6]. However, it's very difficult to prepare large-area n-type conductive diamond, which significantly obstacles the application of diamond in the field of electronic devices [7–9]. The phase transition from graphite under high temperature and high pressure is one of the important ways to prepare diamond, while its size cannot meet the requirements. Many researchers have doped various dopants including nitrogen [10–13], sulfur [14–16], and phosphorus [7,8,17–19] into single or polycrystalline diamond to prepare n-type diamond, but the success is very limited. Due to the surface effect and small size effect, nano-sized diamonds possess greater potential in n-type doping, which has been confirmed by experiments and theoretical calculations [20–24]. These nano-sized diamonds were normally inserted into non-diamond carbon matrix containing amorphous carbon, *trans*-polyacetylene (TPA) and nano graphite, forming nanocrystalline diamond (NCD) films, exhibiting n-type conductivity with high mobility after oxygen or phosphorus ions implantation and 900 or 1000 °C annealing [21–23,25]. Even though the mobility values of these ion implanted NCD films were much larger than those of nitrogen-doped NCD films synthesized by CVD [26,27], the existence of non-diamond carbon decreased the electrical properties and brought obvious shortage in the performance of the NCD-based devices. So, a structure, in which nano-sized diamond grains closely pack each other without non-diamond phase, will improve the electrical properties. However, there is no report about this structure and its electrical properties.

Here, we prepared this microstructure by performing high temperature annealing on the oxygen ion implanted NCD films. It was found that the grain boundaries consisting of amorphous carbon, TPA and nano graphite in NCD films were totally transited to diamond under ordinary pressure and therefore nanocrystalline diamond grains closely packed, named closely-packed nanocrystalline diamond (CPND) films. This transition is an unusual phenomenon because it generally occurred under high pressure and high temperature [28–31]. The CPND films exhibit higher mobility of 522 $cm^2\ V^{-1}\ s^{-1}$ n-type conductivity than those films with thick non-diamond grain boundaries [21,25,27]. The phase transition and high mobility n-type conductivity were ascribed to monoatomic Ta atoms came from hot filament during deposition process. For Ta supplies electrons to the adjacent graphene layer,

* Corresponding author.
E-mail address: huxj@zjut.edu.cn (X. Hu).
[1] These authors contributed equally to this work.

https://doi.org/10.1016/j.carbon.2022.05.013
Received 25 November 2021; Received in revised form 9 April 2022; Accepted 6 May 2022
Available online 12 May 2022

transforming sp^2 electronic configuration to sp^3 state with energy barrier of −5.38 eV/unit cell and Ta terminated diatomic layer diamond forms a shallow donor energy level of ~0.4 eV. These suggest a new way to prepare large-area diamond with n-type conductivity by transforming large-area graphite via the help of monoatomic Ta.

2. Materials and methods

2.1. Experimental

To prepare the nanocrystalline diamond (NCD) films with few amorphous grain boundaries, we deposited a layer of AlN on silicon wafer to increase the nucleation sites due to its rough surface. Also, this insulated AlN layer can isolate the conduction from the silicon substrate. This thin AlN layer was deposited on silicon wafer by using a physical vapor deposition system. Before deposition, the silicon wafer was ultrasonic treated in acetone, ethanol and deionized water one after another to clean its surface. The sputtering chamber was pumped down to a base pressure of 10^{-4} Pa before deposition. High purity argon and nitrogen gas with flow rates of 17 and 5 sccm were introduced and the sputtering pressure of the chamber was set to 0.8 Pa. The DC power of 100 W was applied to the Al target. Thin AlN film with thickness of ~70 nm was deposited on silicon wafer at room temperature within 15 min.

AlN/Si substrate was pre-treated in ultrasonic abrasion for 1 h in a suspension of diamond powder with a grain size of ~1 μm in acetone. The pre-treated substrate was cleaned in acetone and ethanol for 5 min. NCD films were deposited by using a hot filament chemical vapor deposition (HFCVD) system. The Ta wires were used as heating filaments, which were heated to 2200 °C with a DC power of 4800 W. H_2 gas (~90 sccm) was bubbling through acetone (maintained at 0 °C), and extra amount of H_2 gas (~200 sccm) was introduced into the reaction chamber and its pressure was maintained at 0.8 kPa. The deposition time was 15 min. The as-deposited NCD films were oxygen ion implanted at room temperature with 80 keV and a dose of 10^{12} cm^{-2}. The implanted samples were annealed under 700, 800, 900 and 1000 °C for 30 min with the pressure of 4000 Pa, named as O-700, O-800, O-900 and O-1000, respectively.

2.2. Characterizations

The surface morphology and the thickness of each layer were characterized using field emission scanning electron microscopy (FESEM; Nova NanoSEM 450). The crystallization of AlN films was characterized by X-ray diffraction (XRD; Ultima IV). The electrical properties of the films were measured by Hall effects measurements (LakeShore 8400) at room temperature. The R-T test was performed by Quantum Design PPMS-9, and the excitation current was 5 μA. The composition of the films was analyzed by visible (532 nm) and UV (325 nm) Raman spectroscopy (Renishaw inVia Reflex). The microstructure of the films was characterized by high resolution transmission electron microscopy (HRTEM; Tecnai G2 F30 S-Twin). The energy dispersive X-ray spectroscopy (EDX) mapping was obtained on Titan G2 80–200 ChemiSTEM, FEI. The element distribution depending on the depth was acquired by secondary ion mass spectrometry (SIMS) on TOFSIMS5.

2.3. Calculation method

Periodic slab model was used to calculate the transition between graphene and diamond. In this model, both two layers of graphene with AB stacking form lied in the xy-plane above a bulk diamond with (111) surface terminated by hydrogen and separated by 10 Å along z direction. Graphene layers were single-side hydrogenated or double-side partially hydrogenated, and tantalum atoms were added between bulk diamond and graphene layers. The generalized gradient approximation (GGA) of the Perdew-Burke-Ernzerhof (PBE) exchange correlation functional was used to calculate all structural relaxation and electronic structures, as implemented in the Vienna Ab initio Simulation Package (VASP, version 5.4.4) containing the projector augmented wave (PAW) pseudopotential method. Meanwhile, the partial density of states (DOS) with denser k meshes of 9 × 9 × 1 was performed by using PBE exchange-correlation potential after structures reaching the required accuracy. The first-principles based nudged elastic band (NEB) method was applied to calculate the transition barrier, in which it was used to find saddle points and the minimum energy paths between the known reactants and products. The method worked well by optimizing a number of intermediate images along the reaction path. The structural relaxation and transition path optimization were performed within the framework of DFT as implemented by VASP. The charge density difference $\Delta\rho$ is computed by the formula $\Delta\rho = \rho_{Ta + surf + graphene} - \rho_{Ta} - \rho_{surf} - \rho_{graphene}$, where $\rho_{Ta + surf + graphene}$ is the charge density of the diamond surface with Ta atom and two graphene layers, ρ_{Ta}, ρ_{surf} and $\rho_{graphene}$ are the charge densities of isolated Ta atom, the pristine hydrogen-terminated diamond surface and two graphene layers, respectively. The cutoff energy for the expansion of wavefunction into plane waves was set to 600 eV and integrations over the Brillouin zone were performed using the MonkhorstePack scheme. Computation stops when the change in total energy is smaller than 0.1 meV.

3. Results and discussion

To absolutely remove the grain boundaries in NCD films, in addition to annealing under an appropriate temperature, it is necessary to prepare the as-deposited sample with smaller number of grain boundaries comparative with normal NCD films. This needs to increase the nucleation density of nano-sized diamond in the initial growth of the film. To achieve this, we used silicon wafer deposited by aluminum nitride (AlN) layer mainly with (100) crystal orientation as the substrate, whose rough surface will supply much more nucleation sites, see Fig. S1 A-B. Its resistivity exceeds the measuring range of a four-point resistivity measurement facility (10^5 Ω cm), isolating the conduction from the silicon wafer. This ensures that the Hall effects results are attributed to the NCD films with continuous, dense and typical granular morphology (see Figure S1 C). The conductivity of as-deposited diamond film is p-type, while it exhibits n-type when annealing temperature attains to 800 °C and above, see Table 1. This conductivity type transition is in a good agreement with that of oxygen ion implanted nanocrystalline diamond and graphene nanoribbons composited films [23,25]. With annealing temperature further increasing to 1000 °C (named O-1000), the Hall mobility dramatically increases from 16.6 to 522 cm^2 V^{-1} s^{-1}, see Table 1. This carrier mobility value is larger than that of O^+-implanted NCD films not grown on AlN [23], higher dose O^+ or P^+-implanted films [21,22] and nitrogen-doped films synthesized by CVD [26,27]. Moreover, the temperature-dependence line on resistivity of samples O-1000 and O-900 were measured and shown in Fig. S2. The resistivity of the samples gradually increases with the decrease of the test temperature, showing semiconductor characteristics. Meanwhile, in Fig. S2(a), it is observed that at low temperature of about 60–90 K, the main mechanism is the variable-range-hopping conduction for both O-1000 and O-900 samples. The inset image in Fig. S2 shows the temperature dependence of the resistivity as $\ln(\rho) \propto T^{-\frac{1}{4}}$ to verify the variable-range-hopping conduction [32,33]. With the temperature increase to 120 K, the conductance of sample O-900 is mainly nearest-neighbor-hopping conduction with the activation energy of 5 meV and due to the saturation of hopping conduction, the resistivity changed slightly nearly without activation energy at temperature range of 180–300 K. Meanwhile, sample O-900 shows a low carrier mobility of 48.2 cm^2 V^{-1} s^{-1} at room temperature, see Table 1, indicating that the conductance is mainly hopping conduction. For sample O-1000, in temperature range of 90–140 K, the conductance is mainly nearest-neighbor-hopping conduction with the activation energy of 10.9 meV [32,33]. At higher temperature (180–300 K), the activation

Table 1
Room temperature Hall effects results of samples.

Sample	T_a (°C)	Resistivity (Ω·cm)	Hall coefficient (m^2C^{-1})	Hall mobility ($cm^2 \cdot V^{-1} \cdot s^{-1}$)	Sheet carrier concentration (cm^{-2})
As-deposited	–	0.36	50.7	40.4	2.00×10^{17}
O-700	700	0.76	103	40.8	6.04×10^{16}
O-800	800	0.47	−25.8	16.6	-2.41×10^{17}
O-900	900	0.21	−33.5	48.2	-1.86×10^{17}
O-1000	1000	0.22	−390	522	-1.60×10^{16}

energy calculated from the temperature dependence of resistivity increases to 40.9 meV, which is much larger than that of sample O-900 in the same temperature range, suggesting that the conductance of the O-1000 sample is not mainly from hopping, but ascribed to band conduction. The carrier mobility of O-1000, 522 $cm^2\ V^{-1}\ s^{-1}$, is much higher than that of O-900, 48.2 $cm^2\ V^{-1}\ s^{-1}$, which further confirming the band conduction mechanism of sample O-1000, for band conduction generally has a much higher mobility than hopping conduction [32,33]. Also, in Fig. S2 (b), we further analyze the curve of temperature dependence of resistivity to distinguish the hopping conduction and band conduction. We extend the nearest-neighbor-hopping conduction part of the curve for sample O-1000, as the blue line. It is observed that when temperature is higher than 140 K, if the hopping conduction still gives main contribution to the conductance and no other conduction mode appears, the resistivity value will decrease from point A to point B. Here, due to the band conduction appearing, the resistivity value exactly decreases from point A to point C. As we can see in Fig. S2(b), even if the hopping conduction still contribute to the conductance, it is a small part (line AB) and band conduction is the main part (line BC). Therefore, at room temperature, we conclude that the main conduction mechanism is n-type band conduction, not hopping conduction for sample O-1000. It is reported that sp^2 carbon in the grain boundaries of NCD films will cause the film to exhibit n-type conductivity with the activation energy of less than 10 meV [34], and the activation energy of oxygen-doped diamond is 320 meV [35,36]. This indicates that the other components play a key role in the conductance of sample O-1000. Both Hall and R-T measurements also suggest that there are prominent changes in microstructure and composition of sample O-1000, other than those occurred in the normal O^+-implanted NCD samples. To find them, we analyze the phase composition and the microstructure of the as-deposited sample and O-1000 sample.

Fig. 1 A shows that diamond grains are uniformly distributed in the as-deposited film with grain size about 7–15 nm surrounded by grain boundaries with thickness of ~1–2 nm, showing the typical features of NCD films. The inset in Fig. 1A shows its selected area electron diffraction pattern (SAED), which contains (111), (220), (311) and (331) diffraction ring, signifying the small and randomly oriented diamond grains in NCD films. There is also a ring corresponding to the (200) plane of n-diamond, a metastable form of diamond [37]. A prominent diffused ring exists in the centre of SAED pattern, indicating that the grain boundaries are mainly amorphous.

Fig. 1B shows irregular shape of diamond grains with larger size (10–25 nm) and continuous bright lines network in sample O-1000. Its SAED pattern shows three diffraction rings corresponding to (111), (220) and (311) lattice planes of diamond. The numbers of bright spots in the diffraction rings are less than those in as-deposited sample, illustrating that diamond grains in O-1000 sample trend to be the same orientations during annealing. And (200) plane of n-diamond disappears here meaning that the metastable form transits to the stable form, cubic diamond. The interfaces here are observed between diamond grains with thickness in atomic scale and the grain boundaries similar with that in as-deposited sample are nearly not found, indicating that the content of amorphous phase in grain boundaries dramatically decreases, further confirmed by the weakening of the diffused ring in the center of SAED pattern. These lead to much higher intensity of diamond peak of O-1000 sample in UV Raman (see Fig. S1). The growth of diamond and disappearing of grain boundaries indicates that grain boundaries transit to diamond, increasing the diamond content and improving the n-type electrical properties.

High resolution TEM images of these two samples in Fig. 1C and **D** further confirm this phase transition. Fig. 1C shows a typical region of Fig. 1A and diamond grains here are globular, size in ~8 nm, and the grain boundaries with thickness about 2 nm. The Fourier-transformed (FT) diffractogram in the inset FTc shows that several diffraction spots are originated from the diamond grains. In image I and III, the lattice fringes of diamond grains show different orientations with the same interplanar spacing ~0.209 nm corresponding to diamond (111) plane confirmed by images FT_I and FT_{III}. Image II shows that the grain boundaries are amorphous phase contained some nanographite confirmed by image FT_{II} (diffraction ring of graphite was marked by

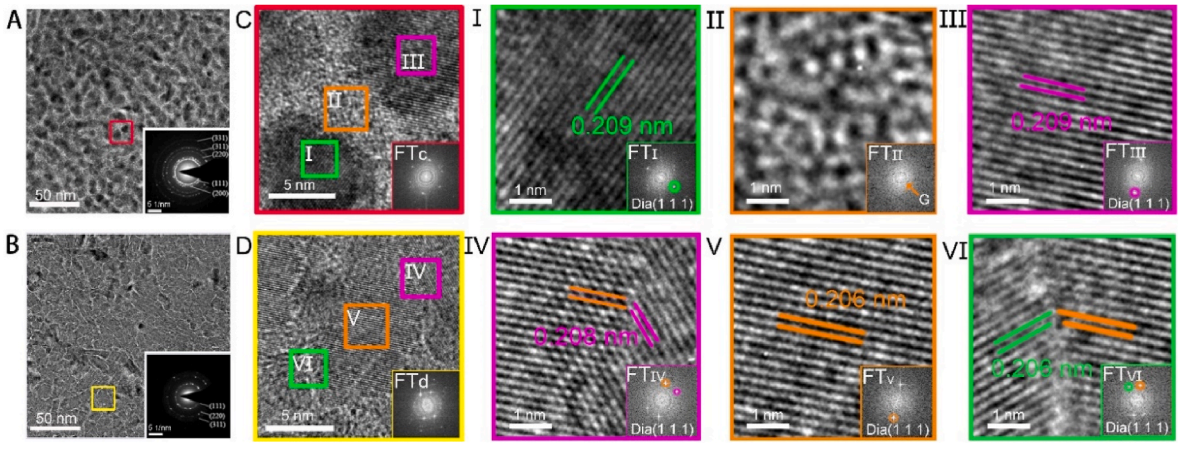

Fig. 1. The microstructure evolution from as-deposited sample to O-1000 sample. Bright field TEM micrographs of **(A)** as-deposited NCD films and **(B)** O-1000 sample with corresponding SAED patterns in the insets. The high-resolution TEM images of **(C)** as-deposited NCD films and **(D)** O-1000 sample with Fourier-transformed diffractograms FTc and FTd in the inset, respectively. Images I, II and III, and images IV, V and VI are the enlarged images with their Fourier-transformed diffractograms of corresponding squares in (C) and (D), respectively. (A colour version of this figure can be viewed online.)

orange arrow).

Fig. 1D shows a random region of sample O-1000 which contained several diamond grains with irregular shape. Image IV shows grain boundaries between right and middle grains, in which no thick grain boundaries but a bright line is observed in Fig. 1D, suggesting that the bright line is the interface of two grains. The lattice fringes of diamond grains reveal the same interplanar spacing ~0.206 nm corresponding to diamond (111) plane confirmed by image FT_{IV}. Image V shows the diamond grain in the middle, displaying very sharp diffraction spots of (111) plane. Image VI shows that the thickness of grain boundaries between left and middle grains is close to 0.2 nm. It was considered that few amorphous phases were in such thin grain boundaries confirmed by its FT image.

In a word, the thick grain boundaries in as-deposited sample transit to the interface of two grains or thin grain boundaries in atomic scale comprised of little amorphous phase. And globular grains transform to irregular, larger and closely packed grains during the annealing. These results confirm that grain boundaries nearly totally transit to diamond after 1000 °C annealing without a high pressure, forming CPND film. These results further clarify that the as-deposited sample with thick grain boundaries shows hopping conduction and O-1000 sample mainly composed of crystals shows band conduction at room temperature.

To explain this unusual phase transition, the change in sp^2 bonded carbon was characterized by visible Raman spectroscopy shown in Fig. S3. The peaks at 1550–1570 and 1340 cm^{-1} correspond to the broad and strong G band and D band, which is originated from the small size effect, large amount of interface and surface zones in the films [38,39]. It is also observed that there are two peaks at 1140–1190 and 1480 cm^{-1} ascribed to the C–H bending and C═C stretching vibrations of TPA chains situated at the grain boundaries in the as-deposited sample [40]. We find that the hydrogen desorbs from TPA in grain boundaries and the content of TPA chains dramatically decreases after 1000 °C annealing (see Fig. S3 and its detailed description), which produces graphene layers in NCD films proved in our previous report [25]. Also, the graphitization of amorphous carbon phase in grain boundaries was often observed in NCD films obtained by microwave plasma CVD after annealing process [41,42]. In addition, it was reported that the graphitization of amorphous carbon was completed with the presence of transition metals Fe and Zn when the temperature is lower than 1000 °C [43,44]. We believe that the graphitization of amorphous carbon in our samples occurs under the conditions of 1000 °C annealing and the existence of the transition metal Ta (see Fig. 2D). In summary, the graphitization of TPA and amorphous carbon, main component of grain boundaries, is easy to occur in our experimental conditions. Moreover, in CPND film (O-1000 sample), nearly all grain boundaries transit to diamond, meaning that after graphitization, graphene layers/nanographite further transits to diamond during 1000 °C annealing.

In order to find the key factors in this transition, more detailed element distribution and microstructural information were examined by performing secondary ion mass spectrometry (SIMS), high angle annular dark field (HAADF) technique and energy dispersive X-ray spectroscopy (EDX) mapping, as shown in Fig. 2. Fig. 2A shows the element depth profile of O-1000 sample. CPND films/AlN/Si structure of O-1000 sample is approximately determined relying on the intensity changes of C, Al and Si, main elements of each layer, marked by brown line. It is observed that the ratio of carbon to hydrogen is relatively stable, and the count of hydrogen has a high value even though it is lower than that of carbon. This demonstrates that main composition of the film, diamond, was hydrogenated. Al, N and Si can be detected in the diamond layer owing to the diffusion of the AlN layer and the silicon substrate during the annealing process. More importantly, it is observed that there are Ta atoms existing in the film, which comes from the Ta filament using as the heat source in CVD system.

The HAADF image shows the geometry and distribution of diamond grains (see Fig. 2B) and the EDX mapping images of C, Ta, N, Al and Si in the same region are shown in Fig. 2C–G, respectively. The atomic percentages of Ta, N, Al and Si are 0.86%, 1.91%, 0.05% and 3.73%, respectively. The N and Al (Fig. 2E and F), present a diffuse distribution in the full images and obviously have no correlation with the granular geometry and distribution of diamond grains shown in Fig. 2B. Si, Fig. 2G, shows the similar distribution with diamond grains but it does not show granular geometry as Fig. 2B. In order to better illustrate the relationship between the distribution of Ta and diamond grains, we have marked some of them by several ellipses in HAADF image and EDX mapping of Ta. As can be seen in Fig. 2B and D, Ta shows the similar distribution and geometry as diamond grains, indicating that Ta may surround the diamond grains for its atomic size is too large to enter diamond crystals. In addition, taking a 10 nm cubic diamond particle as an example, the number of carbon atoms in a 10 nm diamond structure is about 175000. Even if we assume that Ta atoms are uniformly distributed on the surface of each nanodiamond, the atomic percentages of Ta would be 2.7% much higher than 0.86%, implying Ta is dispersed atoms rather than crystal. In the aforementioned TEM results, both Ta crystals and its diffraction information have not been found in the bright field image and SAED image, confirming that they are Ta atoms rather than Ta crystals. This implies the critical influence of Ta atoms on the phase transition and the formation of the closely packed structure of O-1000 sample.

Above results show several important information. First is the desorption of hydrogen from TPA and hydrogen terminated diamond; second is the conversion from amorphous carbon and TPA to graphite and the vanishment of the graphite in grain boundaries; third is that diamond grains become larger and closely packed; forth is Ta atoms surrounding the diamond grains. Thus, it is graphite transformed from amorphous carbon and TPA and nanographite originally existed in grain boundaries that transit to diamond, leading to the formation of the closely packed structure of O-1000 sample. It is well known that normally under atmospheric/low-pressure and 1000 °C conditions, it is

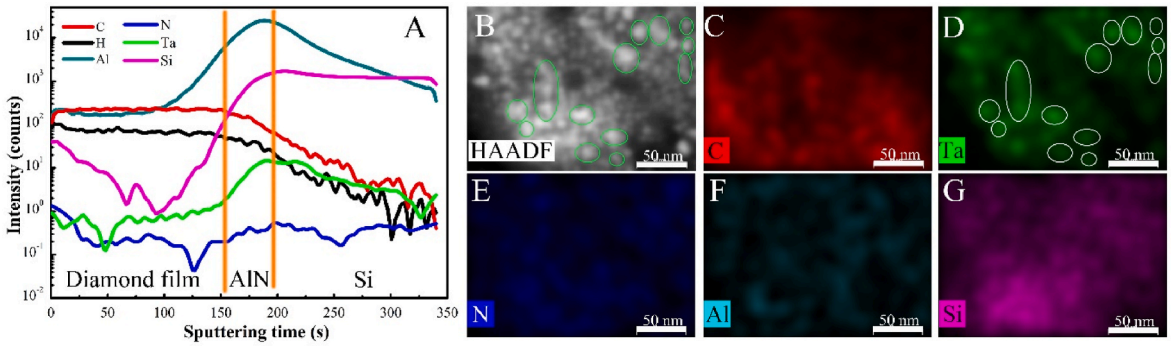

Fig. 2. Elements distribution in the O-1000 sample. (A) The SIMS spectrum and **(B)** the HAADF image of O-1000 sample; **(C)–(G)** EDX mapping information of C, Ta, N, Al and Si, respectively. (A colour version of this figure can be viewed online.)

unlikely that graphite will be converted to diamond. Nevertheless, this phase transition occurs under this condition in our experiments, indicating that there must be other factors that affect the phase transition. According to the composition and element distribution, Ta may play a key role in this phase transition.

We performed first-principles based nudged elastic band (NEB) [45–47] calculations to study the transition possibility from two graphene layers to the diatomic layer diamond and the role of Ta. Fig. 3A shows a transition path from two graphene layers in which one layer of graphene is single-side hydrogenated to the diatomic layer diamond. The four structure images in Fig. 3A correspond to the initial, fourth, sixth and final step in the reaction barrier curve with Ta atoms in Fig. 3B (red line). At the initial stage of transition, single-side hydrogenated graphene layer (SSHG) and graphene layer approach each other (see Fig. 3A 0–4); energy decrease slightly (red line in Fig. 3B). Then the graphene layer affected by the approaching dangling bond, puckers and transforms from sp^2 to sp^3 electronic configuration state (see Fig. 3A 4–6); energy dramatically decrease by 2 eV (red line in Fig. 3B). Finally, C–C bonds are formed between two layers, so that the SSHG and graphene layers polymerize to diatomic layer diamond (see Fig. 3A 6–9); energy further decrease by more than 3 eV (red line in Fig. 3B). The calculated activation barrier shown in Fig. 3B is 0.82 eV/unit cell for the model without Ta atom (black line), meaning that this reaction needs additional conditions, such as high pressure, to overcome the barrier [48,49]. When Ta atom is added, the activation barrier dramatically decreases from 0.82 to −5.38 eV/unit cell (red line in Fig. 3B). This is a great drop, compared with the drop from 0.3 to −1.34 eV in the model added Co (0001) as the substrate to transform multilayer graphene into continuous ultrathin sp^3-bonded carbon films [50]. This means that Ta atom dramatically lowers the activation energy, allowing the reaction proceed spontaneously.

To investigate how the Ta atom reduces the activation barrier, the charge density difference $\Delta\rho$, for images 0, 4, 6, 9 in Fig. 3A, are calculated according to the formula in supporting information and illustrated in Fig. 3C–F. It is clearly observed, in Fig. 3C, that strong electron accumulation occurs between Ta atom and graphene layer. These results indicate that electrons are transferred from diamond surface and graphene to Ta atom. The calculated Bader charge for Fig. 3C and F listed in Table S1 indicates that Ta atom supplies about 0.916 electrons to the underlying diamond surface and graphene layer, majority of which (0.767 e) transferred to graphene layer in Fig. 3C, meaning that Ta has a great influence in the charge distribution of graphene layer. The electron accumulation and depletion are hexagonal shape underlying the six-membered ring of graphene shown in the top-view of Fig. 3C, meaning that Ta atom has nearly equal effects to the six carbon atoms. Fig. 3D shows that after SSHG approaching the graphene

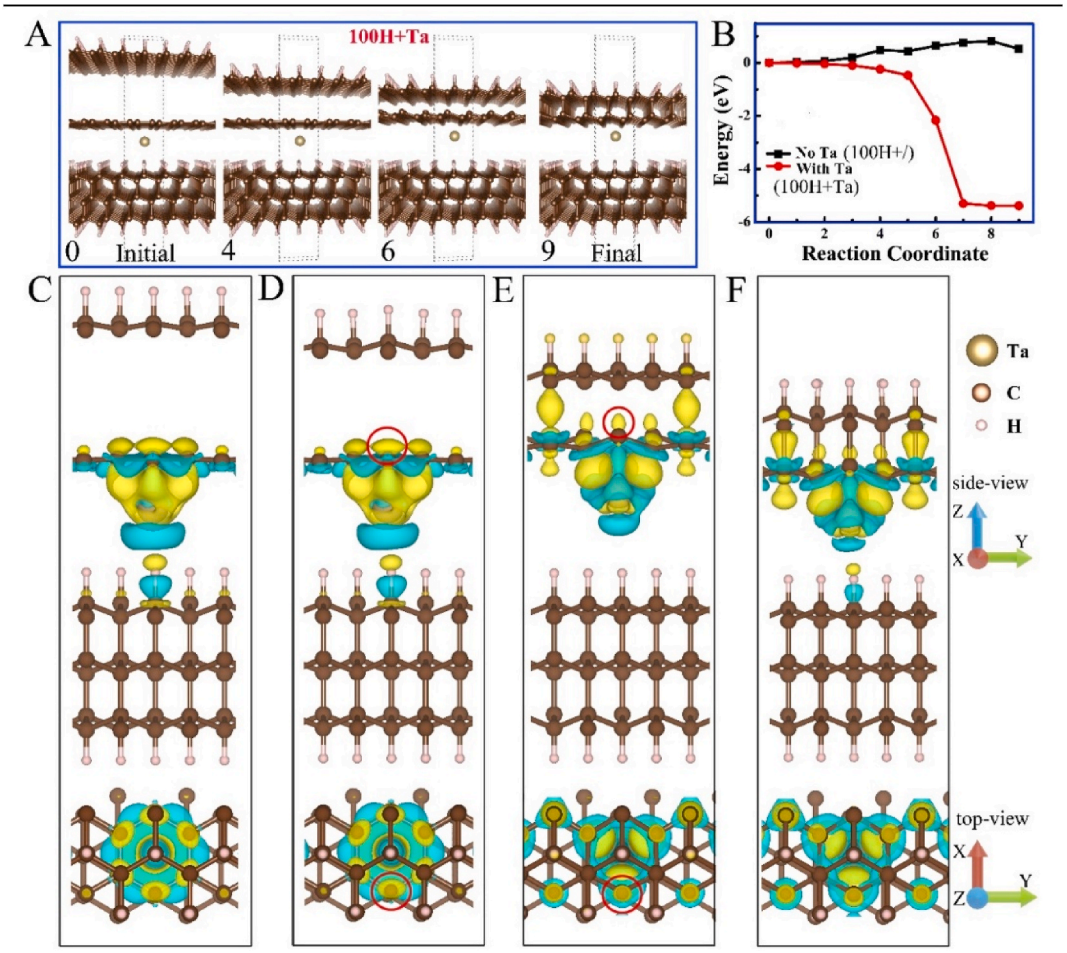

Fig. 3. The plausible transition path from graphene to diatomic layer diamond and the evolution of charge density differences. (A) Calculation model of NEB. Images 0, 4, 6 and 9 are critical intermediate images along the reaction path corresponding to the reaction coordinate 0, 4, 6 and 9 in **(B)**. **(B)** The calculated activation barrier. The transition barrier of model one, in which one-side of graphene was fully hydrogenated and another side was empty (named as 100H+/), is 0.82 eV (black line). The barrier of the other model, in which one-side of graphene was fully hydrogenated and another side was terminated by Ta (named as 100H + Ta), is −5.38 eV. (red line). **(C)**, **(D)**, **(E)** and **(F)** display the charge density differences for structure images 0, 4, 6 and 9 in **(A)**, respectively. The yellow and light blue regions represent the electron accumulation and depletion, respectively. The isosurface values are 0.0034 e/Å^3. (A colour version of this figure can be viewed online.)

layer for a short distance, charge density difference has hardly changed corresponding to the tinily changed activation barrier from 0 to 4 in Fig. 3B. In Fig. 3E, as the SSHG and graphene layer get closer, electron accumulation around Ta atom transforms from hexagonal to triangular (top-view). The three main electron accumulations are below three downwardly shifted carbon atoms in the six-membered ring of graphene (side-view). Meanwhile, carbon atoms in graphene layer are no longer in the same plane and the top-view shows that the electron accumulation of carbon transforms from oval to circle, marked by the red circle shown in Fig. 3D and E, meaning the transition from sp^2 bond to sp^3 bond. In Fig. 3F, Ta atom supplies about 1.317 electrons, major of which (1.202 e) transferred to the adjacent carbon layer of diatomic diamond, much larger than that (0.767 e) in Fig. 3C. These results demonstrate the impact of Ta atom on electron distribution of graphene layer before this transformation. And the formation of triangular electron accumulation shape around Ta atom during this transformation results in a very low activation barrier (Movie. S1 shows this transition process).

Supplementary video related to this article can be found at https://doi.org/10.1016/j.carbon.2022.05.013.

In view of the unique electron transfer features of Ta atom in this transformation, we analyze the electron localization function (ELF) to better understand the bonding nature and how it affects the activation barrier, as shown in Fig. 4 and Fig. S4. Before the formation of the diatomic layer diamond, Ta atom does not bond with carbon, but it has affected the bonding state of graphene layer (see Fig. S4) and the black square area in Fig. 4A, B and 4C shows the bonding state of SSHG. The downwardly shifted carbon atoms show a common dangling bond in the structure without Ta in Fig. 4A. After the Ta atom added, even the SSHG layer is far away from graphene layer and Ta atom, the dangling bonds on SSHG present a tendency to bond with graphene layer, as shown in Fig. 4B. During the approaching of SSHG layer, this trend becomes more obvious, as shown in Fig. 4C. This means that Ta not only affects the bonding state of the graphene layer but also affects the SSHG layer, leading to the trend of bonding between the SSHG and the graphene layer. These results can explain why the energy in Fig. 3B shows a downward trend from image 0 to image 4.

After the formation of diatomic layer diamond, we find that in the absence of Ta, not only each underlying carbon atom has a dangling bond, but also the carbon-carbon bond formed between SSHG layer and graphene layer is very weak (red circle in Fig. 4G), consistent with Fig. S4N. After Ta added, the carbon with dangling bonds bonded with Ta, and the carbon-carbon bond between SSHG layer and graphene layer is strengthened (red circle in Fig. 4H). Moreover, comparing the ELF map of diamond region (see Fig. 4I), especially the area in red circle, we find that the bonding state of diatomic layer diamond after adding Ta is very close to that of bulk diamond. This makes graphene transit to diamond under ordinary pressure.

Experimentally, there will be various hydrogenation states rather than one-side fully hydrogenated graphene in the films. Erohin et al. [51] showed that the higher hydrogenation ratio, the lower phase transition barrier. Also, there are several works indicating that higher hydrogenation ratio of the graphene can reduce the diamondization pressure and temperature [52–55]. Therefore, to further demonstrate the role of Ta in the phase transition process, we calculated another two models, '100H + 50H' and '100H + Ta50H', in which higher hydrogenated ratio was designed (see Fig. S5). Sort according to the energy barrier, (100H+/, 0.82 eV) > (100H + 50H, −4.21 eV) > (100H + Ta, −5.38eV) > (100H + 50HTa, −7.15 eV) (see Fig. 3 and Fig. S5). This indicates that Ta is more conducive to the conversion than hydrogen. We also do the calculation for the transition of graphene films thicker than two layers. The results show that when there is no Ta, the conversion from three layers graphene to diamond is almost impossible (very high

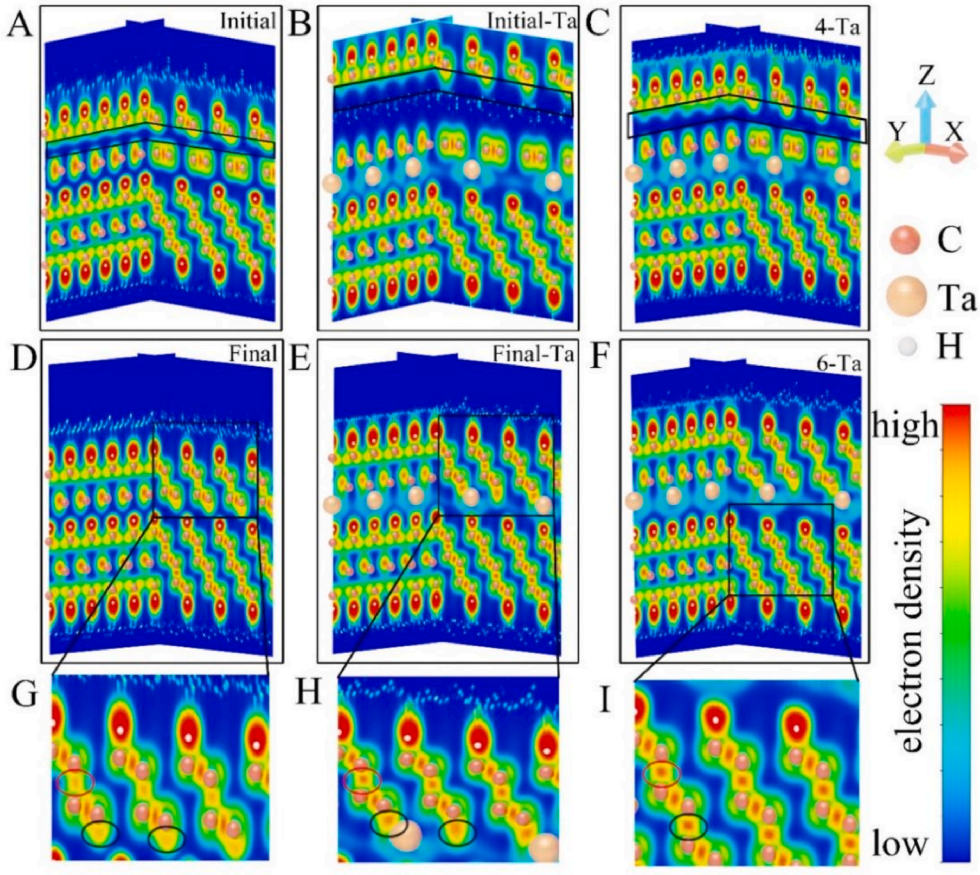

Fig. 4. Evolution of electron localization function (ELF) of structure with Ta and without Ta. ELF maps for initial structure **(A)** without Ta atom and **(B)** after Ta added, and final structure **(D)** without Ta and **(E)** after Ta added; **(C)** and **(F)** are the transition states between **(B)** and **(E)**. The perspective ELF maps shown in the bottom of **A-F** was combined by ELF maps sliced along y-z plane and x-z plane. **(G)–(I)** The enlarge images of the black square area in **(D)–(F)**, respectively. (A colour version of this figure can be viewed online.)

barrier), as shown in Figs. S6c and S6d. Adding Ta makes this transformation possible, see Figs. S6a and S6b. Our experiments have also proved that there is almost no graphene in the CPND films (sample O-1000), indicating that it has been completely converted. That is, regardless of the hydrogenation ratio of graphene, completely conversion occurs under the action of Ta. Based on the development of large-area graphene and graphite [56], our results give a way to prepare large diamond by transiting from graphite.

The calculated results also show that Ta terminated diatomic layer diamond produces an energy level closing to the conduction band 0.4 eV (see Fig. S7), giving contribution to the n-type conductivity. R-T measurements indicate that the activation energy of the CPND film (sample O1000) is 40.9 meV, which is less than the theoretically calculated value 0.4 eV of Ta terminated diatomic layer diamond. This suggests that the complicated surface of nano-sized diamond grains, such as defects and a small amount of sp^2 carbon originated from the interfaces produced by grains closely packing, decreases the activation energy. Thus, we conclude that the Ta terminated irregular diamond grains which are closely-packed in NCD films, form a Ta-doped CPND films with high mobility of 522 $cm^2\ V^{-1}\ s^{-1}$ and low activation energy.

4. Conclusions

In summary, we find a monoatomic Ta induced phase transition from graphite to n-type diamond under ordinary pressure. This diamondization under normal pressure supplies a method to prepare large-area diamond from graphene or graphite. This also supplies very important significance in the preparation of diamond-based electronic devices due to the synthesis of high-quality n-type CPND films. Our results give solutions to the two major challenges of large-area diamond and n-type diamond in the field and open a way for the matter with different hybridization to transit sp^2 to sp^3 electronic configuration via the help of a single atom.

Data availability

The data that support the findings of this study are available within the article and its supplementary material.

CRediT authorship contribution statement

Chengke Chen: Investigation, Data curation, Writing – original draft, Visualization. **Dong Fan:** Investigation, Data curation, Writing – original draft. **Hui Xu:** Investigation, Data curation. **Meiyan Jiang:** Writing – review & editing. **Xiao Li:** Writing – review & editing. **Shaohua Lu:** Writing – review & editing. **Changcheng Ke:** Investigation, Data curation. **Xiaojun Hu:** Funding acquisition, Conceptualization, Supervision, Writing – review & editing.

Declaration of competing interest

The authors declare that they have no known competing financial interests or personal relationships that could have appeared to influence the work reported in this paper.

Acknowledgements :

Key Project of National Natural Science Foundation of China (Grant No. U1809210) and National Natural Science Foundation of China (Grant Nos. 52102052, 50972129 and 50602039); Key Research and Development Program of Zhejiang Province (2018C04021); International Science and Technology Cooperation Program of China (2014DFR51160); National Key Research and Development Program of China (No. 2016YFE0133200); European Union's Horizon 2020 Research and Innovation Staff Exchange (RISE) Scheme (No. 734578).

Appendix A. Supplementary data

Supplementary data to this article can be found online at https://doi.org/10.1016/j.carbon.2022.05.013.

References

[1] W. Zhu, G.P. Kochanski, S. Jin, Low-field electron emission from undoped nanostructured diamond, Science 282 (5393) (1998) 1471–1473.
[2] M.W. Geis, N.N. Efremow, K.E. Krohn, J.C. Twichell, T.M. Lyszczarz, R. Kalish, et al., A new surface electron-emission mechanism in diamond cathodes, Nature 393 (6684) (1998) 431–435.
[3] W.Y. Liu, M. Tagawa, H.L.L. Xin, T. Wang, H. Emamy, H.L. Li, et al., Diamond family of nanoparticle superlattices, Science 351 (6273) (2016) 582–586.
[4] H. Watanabe, C.E. Nebel, S. Shikata, Isotopic homojunction band engineering from diamond, Science 324 (5933) (2009) 1425–1428.
[5] M.A. Plano, M.I. Landstrass, L.S. Pan, S. Han, D.R. Kania, S. McWilliams, et al., Polycrystalline CVD diamond films with high electrical mobility, Science 260 (5112) (1993) 1310–1312.
[6] J.E. Graebner, S. Jin, G.W. Kammlott, J.A. Herb, C.F. Gardinier, Large anisotropic thermal-conductivity in synthetic diamond films, Nature 359 (6394) (1992) 401–403.
[7] H. Kato, M. Ogura, T. Makino, D. Takeuchi, S. Yamasaki, N-type control of single-crystal diamond films by ultra-lightly phosphorus doping, Appl. Phys. Lett. 109 (14) (2016) 5.
[8] Y. Balasubramaniam, P. Pobedinskas, S.D. Janssens, G. Sakr, F. Jomard, S. Turner, et al., Thick homoepitaxial (110)-oriented phosphorus-doped n-type diamond, Appl. Phys. Lett. 109 (6) (2016) 4.
[9] D. Saada, J. Adler, R. Kalish, Sulfur: a potential donor in diamond, Appl. Phys. Lett. 77 (6) (2000) 878–879.
[10] A. Aleksov, A. Denisenko, E. Kohn, First epitaxial pnp bipolar transistor on diamond with deep nitrogen donor, Electron. Lett. 35 (20) (1999) 1777–1779.
[11] J.F. Prins, Nitrogen-related n-type conduction with low thermal activation in diamond, Semicond. Sci. Technol. 16 (9) (2001) L50–L52.
[12] J. Birrell, J.E. Gerbi, O. Auciello, J.M. Gibson, D.M. Gruen, J.A. Carlisle, Bonding structure in nitrogen doped ultrananocrystalline diamond, J. Appl. Phys. 93 (9) (2003) 5606–5612.
[13] S. Bhattacharyya, O. Auciello, J. Birrell, J.A. Carlisle, L.A. Curtiss, A.N. Goyette, et al., Synthesis and characterization of highly-conducting nitrogen-doped ultrananocrystalline diamond films, Appl. Phys. Lett. 79 (10) (2001) 1441–1443.
[14] L. Tang, R.F. Yue, Y. Wang, N-type B-S co-doping and S doping in diamond from first principles, Carbon 130 (2018) 458–465.
[15] S. Gupta, B.R. Weiner, G. Morell, Room-temperature electrical conductivity studies of sulfur-modified microcrystalline diamond thin films, Appl. Phys. Lett. 83 (3) (2003) 491–493.
[16] I. Sakaguchi, N. Mikka, Y. Kikuchi, E. Yasu, H. Haneda, T. Suzuki, et al., Sulfur: a donor dopant for n-type diamond semiconductors, Phys. Rev. B 60 (4) (1999), R2139.
[17] S. Koizumi, T. Teraji, H. Kanda, Phosphorus-doped chemical vapor deposition of diamond, Diam. Relat. Mater. 9 (3) (2000) 935–940.
[18] S. Koizumi, Growth and characterization of phosphorus doped n-type diamond thin films, Phys. Status Solidi 172 (1) (1999) 71–78.
[19] H. Kato, S. Yamasaki, H. Okushi, n-type doping of (001)-oriented single-crystalline diamond by phosphorus, Appl. Phys. Lett. 86 (22) (2005).
[20] S.H. Lu, Y.C. Wang, H.Y. Liu, M.S. Miao, Y.M. Ma, Self-assembled ultrathin nanotubes on diamond (100) surface, Nat. Commun. 5 (2014) 6.
[21] X. Hu, J. Ye, H. Hu, X. Chen, Y. Shen, Phosphorus ion implantation and annealing induced n-type conductivity and microstructure evolution in ultrananocrystalline diamond films, Appl. Phys. Lett. 99 (13) (2011), 131902.
[22] X.J. Hu, J.S. Ye, H.J. Liu, Y.G. Shen, X.H. Chen, H. Hu, n-type conductivity and phase transition in ultrananocrystalline diamond films by oxygen ion implantation and annealing, J. Appl. Phys. 109 (5) (2011) 7.
[23] H. Xu, H. Ye, D. Coathup, I.Z. Mitrovic, A.D. Weerakkody, X. Hu, An insight of p-type to n-type conductivity conversion in oxygen ion-implanted ultrananocrystalline diamond films by impedance spectroscopy, Appl. Phys. Lett. 110 (3) (2017), 033102.
[24] S. Lu, D. Fan, C. Chen, Y. Mei, Y. Ma, X. Hu, Ground-state structure of oxidized diamond (100) surface: an electronically nearly surface-free reconstruction, Carbon 159 (2020) 9–15.
[25] X. Hu, C. Chen, S. Lu, High mobility n-type conductive ultrananocrystalline diamond and graphene nanoribbon hybridized carbon films, Carbon 98 (2016) 671–680.
[26] O.A. Williams, Ultrananocrystalline diamond for electronic applications, Semicond. Sci. Technol. 21 (8) (2006) R49.
[27] P. Achatz, O.A. Williams, P. Bruno, D.M. Gruen, J.A. Garrido, M. Stutzmann, Effect of nitrogen on the electronic properties of ultrananocrystalline diamond thin films grown on quartz and diamond substrates, Phys. Rev. B 74 (15) (2006), 155429.
[28] P. Németh, K. McColl, R.L. Smith, M. Murri, L.A.J. Garvie, M. Alvaro, et al., Diamond-graphene composite nanostructures, Nano Lett. 20 (5) (2020) 3611–3619.
[29] Q. Huang, D. Yu, B. Xu, W. Hu, Y. Ma, Y. Wang, et al., Nanotwinned diamond with unprecedented hardness and stability, Nature 510 (7504) (2014) 250–253.
[30] F.P. Bundy, H.T. Hall, H.M. Strong, R.H. Wentorf, Man-made diamonds, Nature 176 (4471) (1955) 51–55.

[31] S.C. Zhu, X.Z. Yan, J. Liu, A.R. Oganov, Q. Zhu, A revisited mechanism of the graphite-to-diamond transition at high temperature, Matter 3 (3) (2020) 864–878.
[32] P. Kordos, M. Morvic, J. Betko, J.M. Van Hove, A.M. Wowchak, P.P. Chow, Conductivity and Hall effect characterization of highly resistive molecular-beam epitaxial GaN layers, J. Appl. Phys. 88 (10) (2000) 5821–5826.
[33] N.F. Mott, Conduction in non-crystalline systems, Philos. Mag. A 17 (150) (1968) 1259–1268.
[34] O.A. Williams, S. Curat, J.E. Gerbi, D.M. Gruen, R.B. Jackman, n-Type conductivity in ultrananocrystalline diamond films, Appl. Phys. Lett. 85 (10) (2004) 1680–1682.
[35] J.F. Prins, n-type semiconducting diamond by means of oxygen-ion implantation, Phys. Rev. B 61 (11) (2000) 7191–7194.
[36] J.F. Prins, The nature of radiation damage in diamond: activation of oxygen donors, Diam. Relat. Mater. 9 (3) (2000) 1275–1281.
[37] J. Peng, J. Orwa, B. Jiang, S. Prawer, L. Bursill, Nano-crystals of c-diamond, n-diamond and i-carbon grown in carbon-ion implanted fused quartz, Int. J. Mod. Phys. B 15 (23) (2001) 3107–3123.
[38] M. Mermoux, S. Chang, H.A. Girard, J.C. Arnault, Raman spectroscopy study of detonation nanodiamond, Diam. Relat. Mater. 87 (2018) 248–260.
[39] J. Wagner, C. Wild, P. Koidl, Resonance effects in Raman scattering from polycrystalline diamond films, Appl. Phys. Lett. 59 (7) (1991) 779–781.
[40] H. Kuzmany, R. Pfeiffer, N. Salk, B. Günther, The mystery of the 1140 cm−1 Raman line in nanocrystalline diamond films, Carbon 42 (5–6) (2004) 911–917.
[41] S.-S. Chen, H.-C. Chen, W.-C. Wang, C.-Y. Lee, I.N. Lin, J. Guo, et al., Effects of high energy Au-ion irradiation on the microstructure of diamond films, J. Appl. Phys. 113 (11) (2013).
[42] S.-C. Lin, C.-J. Yeh, J. Kurian, C.-L. Dong, H. Niu, K.-C. Leou, et al., The microstructural evolution of ultrananocrystalline diamond films due to P ion implantation process—the annealing effect, J. Appl. Phys. 116 (18) (2014), 183701.
[43] C. Liang, Y. Chen, M. Wu, K. Wang, W. Zhang, Y. Gan, et al., Green synthesis of graphite from CO2 without graphitization process of amorphous carbon, Nat. Commun. 12 (1) (2021) 119.
[44] X. Deng, W. Shi, Y. Zhong, W. Zhou, M. Liu, Z. Shao, Facile strategy to low-cost synthesis of hierarchically porous, active carbon of high graphitization for energy storage, ACS Appl. Mater. Interfaces 10 (25) (2018) 21573–21581.
[45] G. Henkelman, B.P. Uberuaga, H. Jónsson, A climbing image nudged elastic band method for finding saddle points and minimum energy paths, J. Chem. Phys. 113 (22) (2000) 9901–9904.
[46] G. Kresse, J. Furthmuller, Efficiency of ab-initio total energy calculations for metals and semiconductors using a plane-wave basis set, Comput. Mater. Sci. 6 (1) (1996) 15–50.
[47] G. Kresse, J. Furthmuller, Efficient iterative schemes for ab initio total-energy calculations using a plane-wave basis set, Phys. Rev. B 54 (16) (1996) 11169–11186.
[48] A.P.M. Barboza, M.H.D. Guimaraes, D.V.P. Massote, L.C. Campos, B.R.A. Neves, Room-temperature compression-induced diamondization of few-layer graphene, Adv. Mater. 23 (27) (2011) 3014–3017.
[49] J. Dong, Z. Yao, M. Yao, R. Li, K. Hu, L. Zhu, et al., Decompression-induced diamond formation from graphite sheared under pressure, Phys. Rev. Lett. 124 (6) (2020), 065701.
[50] D. Odkhuu, D. Shin, R.S. Ruoff, N. Park, Conversion of multilayer graphene into continuous ultrathin sp(3)-bonded carbon films on metal surfaces, Sci. Rep. 3 (2013) 7.
[51] S.V. Erohin, Q. Ruan, P.B. Sorokin, B.I. Yakobson, Nano-thermodynamics of chemically induced graphene-diamond transformation, Small 16 (47) (2020), e2004782.
[52] Z. Zhang, X.C. Zeng, W. Guo, Fluorinating hexagonal boron nitride/graphene multilayers into hybrid diamondlike nanofilms with tunable energy gap, J. Phys. Chem. C 115 (44) (2011) 21678–21684.
[53] S. Paul, K. Momeni, Mechanochemistry of stable diamane and atomically thin diamond films synthesis from Bi- and multilayer graphene: a computational study, J. Phys. Chem. C 123 (25) (2019) 15751–15760.
[54] S. Rajasekaran, F. Abild-Pedersen, H. Ogasawara, A. Nilsson, S. Kaya, Interlayer carbon bond formation induced by hydrogen adsorption in few-layer supported graphene, Phys. Rev. Lett. 111 (8) (2013) 5.
[55] G. Qin, L. Wu, H. Gou, Diamane: design, synthesis, properties, and challenges, Functional Diamond 1 (1) (2021) 83–92.
[56] X.S. Li, W.W. Cai, J.H. An, S. Kim, J. Nah, D.X. Yang, et al., Large-area synthesis of high-quality and uniform graphene films on copper foils, Science 324 (5932) (2009) 1312–1314.